Available online at www.sciencedirect.com
ScienceDirect
International Journal of Heat and Mass Transfer 51 (2008) 3227–3244
International Journal of HEAT and MASS TRANSFER
www.elsevier.com/locate/ijhmt

The heat/mass transfer analogy for a simulated turbine endwall

S. Han, R.J. Goldstein *

Department of Mechanical Engineering, Heat Transfer Laboratory, University of Minnesota, 1200 Mechanical Engineering Building, 111 Church Street S.E., Minneapolis, MN 55455, USA

Received 6 August 2007; received in revised form 9 December 2007
Available online 2 April 2008

Abstract

Heat transfer measurements in gas turbine cascades are often difficult because of thin boundary layers, complex secondary flows, and large variation in local heat transfer rates. Thus mass transfer techniques have often been used as an alternative method, the heat transfer coefficients being then calculated from the heat/mass transfer analogy.

To ensure confidence in the quantitative conversion to the heat transfer coefficients from the mass transfer results, evaluation of the analogy factors is crucial. The present paper examines the validity of the heat/mass transfer analogy, evaluating the analogy factors on a simulated turbine endwall, with separate heat and mass transfer experiments with equivalent flow and geometric conditions. The Nusselt numbers, determined from the heat transfer experiments with a constant wall temperature boundary condition are compared to Sherwood numbers from the mass transfer experiments employing a constant wall concentration boundary condition to evaluate the heat/mass transfer analogy.

Keywords: Heat/mass transfer analogy; Naphthalene sublimation; Thermal boundary layer; Constant temperature; Constant concentration; Turbine endwall

1. Introduction

Mass transfer experiments have been extensively used to determine heat transfer coefficients using the heat/mass transfer analogy. Local mass transfer results can be obtained under laboratory conditions with a high resolution and precision in a short time period. Mass transfer experiments are free from conduction and radiation errors which are inherent in heat transfer studies. However, when precise heat transfer results are required, detailed local heat/mass transfer analogy factors may be required to convert the mass transfer data into heat transfer results.

The heat/mass transfer analogy is derived from the conservation equations of momentum, energy and concentration of a constant property fluid by Nusselt [1] and Schmidt [2]. A heat/mass transfer analogy implies that heat transfer results can be converted from the mass transfer results under equivalent experimental conditions and vice-versa. This follows from the similarity of the equations governing heat and mass transfer.

The non-dimensional heat transfer equation

$$\frac{\mathrm{D}\theta}{\mathrm{D}\tau} = \frac{1}{RePr}\frac{\partial}{\partial \widehat{x}_i}\left(\left(1+\frac{\epsilon}{\nu}\frac{Pr}{Pr_t}\right)\frac{\partial\theta}{\partial \widehat{x}_i}\right) \tag{1}$$

and the non-dimensional mass transfer equation

$$\frac{\mathrm{D}m}{\mathrm{D}\tau} = \frac{1}{ReSc}\frac{\partial}{\partial \widehat{x}_i}\left(\left(1+\frac{\epsilon}{\nu}\frac{Sc}{Sc_t}\right)\frac{\partial m}{\partial \widehat{x}_i}\right) \tag{2}$$

are very similar. Hence, if the boundary conditions are equivalent for a given geometry, if Pr is equal to Sc, and Pr_t is equal to Sc_t, then 'θ' in Eq. (1) and 'm' in Eq. (2) have the same variations. This essentially describes the heat/mass transfer analogy. It should, however, be noted that the Prandtl number in a heat transfer experiment is typically different from the Schmidt number in a mass transfer experiment. Therefore, the usefulness of the heat/mass

* Corresponding author. Tel.: +1 612 625 5552.
E-mail address: rjg@me.umn.edu (R.J. Goldstein).

0017-9310/$ - see front matter © 2008 Elsevier Ltd. All rights reserved.
doi:10.1016/j.ijheatmasstransfer.2008.01.011

Nomenclature

AR	inlet/exit area ratio of the cascade = 2.72
$C_l, (\mathrm{C_L})$	characteristic length, $C_l = 184$ mm in present study
C_x	axial chord length of blade, =130 mm in present study
d	distance from a blade leading edge
D_{naph}	mass diffusion coefficient
F	local analogy factor, $F = Nu/Sh$
H	height of blade = 457 mm
h	heat transfer coefficient
h_{m}	mass transfer coefficient
m	dimensionless mass fraction
M_{naph}	molecular mass for naphthalene, $M_{\mathrm{naph}} = 129.17$ kg/kmol
n	power index used in heat/mass transfer analogy
n	the distance in the direction normal to the wall
Nu	Nusselt number, $Nu = h \cdot C_l/k$
P	pitch of blade, =138 mm
$p_{\mathrm{v,w}}$	naphthalene vapor pressure at the wall
Pr	Prandtl number, $Pr = \nu/\alpha$
Pr_{t}	turbulent Prandtl number, $Pr_{\mathrm{t}} = \epsilon/\epsilon_H$
q_{w}	heat flux from the wall
R	gas constant for naphthalene$(C_{10}H_8), R = 0.06487$ J/g K
$\overline{R}$	universal gas constant
Re_{ex}	exit Reynolds number, $= \rho U_{\mathrm{ex}} C_l/\mu$
S	curvilinear coordinate on the blade
S_{p}	curvilinear coordinate on the pressure surface, cf. Fig. 8
S_{s}	curvilinear coordinate on the suction surface, cf. Fig. 8
Sc	Schmidt number, $Sc = \nu/D_{\mathrm{naph}}$
Sc_{t}	turbulent Schmidt number, $Sc_{\mathrm{t}} = \epsilon/\epsilon_M$
Sh	Sherwood number, $Sh = h_{\mathrm{m}} \cdot C_l/D_{\mathrm{naph}}$
St	Stanton number, $St = \frac{Nu}{RePr} = h/\rho c_p U_\infty$
St_{m}	mass transfer Stanton number, $St_{\mathrm{m}} = \frac{Sh}{ReSc} = h_{\mathrm{m}}/U_\infty$
T_{w}	wall temperature
T_∞	free stream temperature
T_{aw}	adiabatic wall temperature
$T_{\mathrm{n,w}}$	surface temperature of naphthalene
Tu	turbulence intensity, $Tu = \frac{\sqrt{\overline{u'^2}}}{U_\infty}$
U_∞	mainstream inflow velocity in wind tunnel
x	coordinate in blade chord direction
x_i	coordinate along the inflow direction, cf. Fig. 8
y	coordinate traverse to the blade chord direction
Z	coordinate in spanwise direction of cascade, $Z = 0$ at the top

Greek symbols

$\delta\tau$	time duration of data run
δt	sublimation depth of naphthalene
ϵ	turbulent momentum diffusivity
ϵ_H	turbulent thermal diffusivity
ϵ_M	turbulent mass diffusivity
ρ_{s}	density of solid naphthalene
$\rho_{\mathrm{v},\infty}$	naphthalene vapor density in free stream
$\rho_{\mathrm{v,w}}$	naphthalene vapor density at the surface
θ	dimensionless temperature difference
k	thermal conductivity of air

Superscript

$\hat{}$	non-dimensional parameter

Subscripts

atm	atmosphere property
st	static property
w	wall property

transfer analogy requires simple relations for the case of unequal Prandtl and Schmidt numbers.

Lewis [3] showed that the heat and mass transfer coefficients can be accurately related using an expression from universal velocity profiles in a turbulent boundary layer. Chen and Goldstein [4] used $n = 1/3$ to get an analogy factor with the Colburn relation $\frac{Nu}{Sh} = \left(\frac{Pr}{Sc}\right)^n$. Goldstein and Cho [5] reviewed the naphthalene sublimation technique and the heat/mass transfer analogy with a constant heat flux boundary condition. They recommended $n = 1/3$ for a laminar flow and $n = 0.14$ for wake regions in a Colburn type relation. Eckert et al. [6] compared experimental data with the heat/mass transfer analogy for laminar, turbulent, and three-dimensional flow. However, comparison across different studies is difficult due to the different geometric and experimental conditions. Yoo et al. [7] measured local and average mass transfer rates from a rectangular cylinder. They compared the mass transfer results with heat transfer results from a constant heat flux experiment. It was concluded that the discrepancy between heat and mass transfer results comes from the difference in the boundary condition, the effect of 'n' in the Colburn relation, conduction error in heat transfer and mechanical erosion in mass transfer. Apparently, no heat and mass transfer comparisons have been performed with equivalent boundary conditions on the same geometry for the evaluation of the analogy. With a turbulent boundary layer, the effect of different thermal boundary conditions may not be as important as in a laminar flow. However, the constant wall heat flux condition is not equivalent to the constant wall concentration condition and generally results in a higher heat transfer coefficient than the latter. Therefore, a constant wall temperature boundary condition is required to get accurate heat/mass transfer analogy factors when a comparison is to be made with a mass transfer study, with a constant wall concentration boundary condition.

The present paper investigates the validity of the analogy and determines the analogy factor with equivalent boundary conditions on a simulated turbine endwall through heat and mass transfer experiments. For the mass transfer experiment, the naphthalene sublimation technique is employed to obtain local mass transfer coefficients. For the heat transfer experiment, a thermal boundary layer measurement technique is used to obtain local heat transfer coefficients while maintaining the wall at constant temperature.

In a companion paper, the heat/mass transfer analogy on a blade is investigated with similar heat and mass transfer experimental techniques.

2. Extended heat/mass transfer analogy

Eckert et al. [6] indicated three methods of applying the extended heat/mass transfer analogy. One is deduced from the Navier–Stokes equation for a constant property fluid. Another is obtained from empirical expressions of heat and mass transfer equations for a specified flow. The third involves the assumption that local Nusselt numbers are proportional to the local Sherwood numbers with the averaged analogy factor ($\overline{Nu}/\overline{Sh}$).

The Nusselt (Nu) and Sherwood (Sh) numbers are a function of the Prandtl and Schmidt numbers, respectively, in addition to the Reynolds number and the geometry. Their local values can be described as

$$Nu = f(Re, Pr, \hat{x}_i), \quad Sh = f(Re, Sc, \hat{x}_i). \tag{3}$$

For laminar flow on a flat plate, the empirical relation of Eq. (4) is used for obtaining the Nusselt and Sherwood numbers

$$Nu = C_1 Re^m Pr^n, \quad Sh = C_1 Re^m Sc^n. \tag{4}$$

However, the Prandtl number of air in the region studied is ≈ 0.7 while the Schmidt number of naphthalene (in air) is ≈ 2.28. This means that a conversion factor is required to obtain Nu from Sh and vice-versa

$$Nu = F \cdot Sh. \tag{5}$$

Thus, for the same Reynolds number, the analogy factor for a flat plate can be expressed as

$$F = \frac{Nu}{Sh} = \left(\frac{Pr}{Sc}\right)^n, \tag{6}$$

where the exponent 'n' is determined from known solutions. For a laminar flow, $n = 1/3$ is obtained from the solution of the Blasius equations resulting in $F = 0.677$ for $Pr = 0.707$ and $Sc = 2.28$.

For turbulent flow on a flat plate, a Stanton number correlation was developed by Eckert and Drake [8]

$$St = \frac{0.0296 Re_x^{-1/6}}{1 + 1.48 Re_x^{-1/10} Pr^{-1/6}(Pr - 1)}. \tag{7}$$

An analogy factor equation can be obtained from Eqs. (3) and (7)

Table 1
Analogy factors (F) for varying Reynolds numbers

No.	Re_x	Eckert and Drake, Eq. (8)	Kays and Crawford, Eq. (10)
1	1×10^5	0.403	0.548
2	5×10^5	0.393	0.498
3	1×10^6	0.388	0.479
4	5×10^6	0.378	0.440
5	1×10^7	0.374	0.326
6	5×10^7	0.363	0.395

$$F = \left(\frac{Pr}{Sc}\right) \frac{1 + 1.48 Re_x^{-1/10} Sc^{-1/6}(Sc - 1)}{1 + 1.48 Re_x^{-1/10} Pr^{-1/6}(Pr - 1)}. \tag{8}$$

The analogy relation of Eq. (8) results in $F = 0.388$ for $Re_x = 1 \times 10^6$ with $Pr = 0.707$ and $Sc = 2.28$.

Kays and Crawford [9] developed another Stanton number correlation for turbulent flow on a flat plate

$$St = \frac{0.0287 Re_x^{-0.2}}{0.85 + 0.169 Re_x^{-0.1}(13.2Pr - 8.66)}. \tag{9}$$

Another analogy factor equation for a turbulent flat plate is developed from Eqs. (3) and (9)

$$F = \left(\frac{Pr}{Sc}\right) \frac{0.85 + 0.169 Re_x^{-1/10}(13.2Sc - 8.66)}{0.85 + 0.169 Re_x^{-1/10}(13.2Pr - 8.66)}. \tag{10}$$

With $Re_x = 1 \times 10^6, Pr = 0.707$ and $Sc = 2.28$, the analogy factor F is 0.479. The analogy factors are listed in Table 1 for each equation for different Reynolds numbers.

3. Experimental method and setup

The test section, shown in Fig. 1, is connected to the exit of the contraction region of a blowing-type wind tunnel. The bottom endwall has a large opening where the heat or mass transfer endwall can be placed. The top endwall has one rectangular window for the insertion of the thermal boundary layer probe and visual observation. The profile of a modern high performance turbine blade, modified for experimental flow conditions, is used for the blades in the cascade. The straight section of the tunnel, with a cross section of 457 mm × 457 mm and a length of 610 mm, has slots for inserting grid turbulence generators. A 1 mm diameter trip wire is placed near the exit of the contraction section on the bottom endwall (820 mm upstream of the stagnation point of the central blade), to induce a near-fully-developed turbulent boundary layer on the endwall at the inlet to the cascade. The cascade exit flow velocity is calculated using incoming flow velocity and the area aspect ratio (2.72).

3.1. Heat transfer experiment

Local heat transfer coefficients are determined from measurements on a constant temperature endwall with a thermal boundary layer probe. To increase measurement

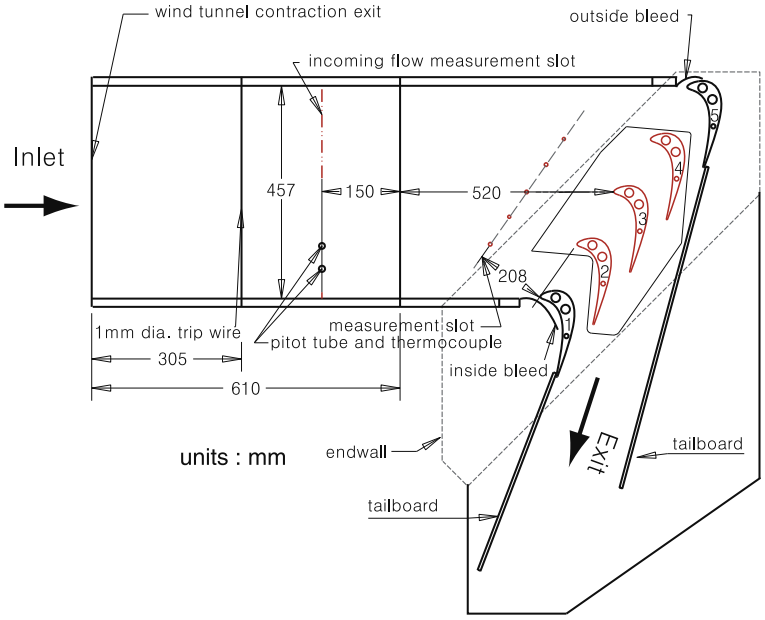

Fig. 1. Test section for the heat and mass transfer experiment.

repeatability and reduce error, a fully automated temperature measurement system was developed at the Heat Transfer Laboratory, University of Minnesota. A detailed description of the heat transfer experiment can be found in Han and Goldstein [10].

3.1.1. Thermal boundary measurement method

Very near the wall, any turbulence fluctuations are small and go to zero at the wall, as does the fluid velocity. The thermal energy is assumed to be transported only by molecular heat conduction in the viscous sublayer region, resulting in a linear temperature variation with distance from the wall. The heat flux can then be evaluated from the thermal gradient as

$$q_w = -k\frac{\partial T}{\partial n}, \tag{11}$$

where n is normal to the surface. Subsequently, the heat transfer coefficient is obtained from the heat flux, wall temperature and free stream temperature

$$h = \frac{q_w}{T_w - T_\infty} = \frac{-k\partial T/\partial n}{T_w - T_\infty}. \tag{12}$$

From Eq. (12), the local Nusselt number is expressed as

$$Nu = \frac{hC_l}{k} = \frac{-C_l\partial T/\partial n}{T_w - T_\infty}. \tag{13}$$

Thus, from Eqs. (12) and (13), the precise evaluation of the heat transfer coefficients and Nusselt numbers depend on the accurate measurement of the temperature in the viscous sublayer region, as well as the freestream and wall temperatures. For this calculation, the wall temperature is obtained by extrapolating the temperatures in the sublayer region. Therefore, one must determine the wall location accurately.

3.1.2. Thermal boundary layer probe

A direct temperature measurement with a micro-thermocouple is used to determine the thermal gradient near the wall. The presence of a probe can disturb the flow and influence the heat transfer measurement. High heat transfer regions can generate large thermal gradients near the wall and cause significant conduction errors in a thermocouple probe. Also, the high velocity of incoming flow can vibrate the probe. Therefore, the special thermal probe is designed to reduce flow disturbance, to minimize the conduction error and to ensure accurate measurement location.

Blackwell and Moffat [11] reviewed temperature measurements using thermocouple probes. They evaluated the performance of various thermocouples for conduction errors and suggested a butt-welded E-type model. For the present study, the junction of the $\phi = 76$ μm E-type thermocouple is butt-welded by an electric discharge welding technique. The thermal probe is shown in Fig. 2. The thermocouple junction is located midway between two hypodermic needles. The exposed part of the thermocouple wire is

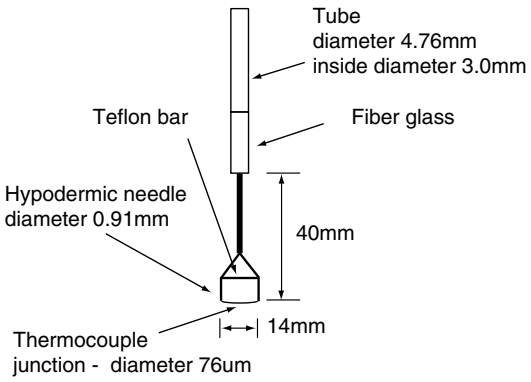

Fig. 2. Thermal boundary layer probe schematic.

14 mm wide and has a slight curvature (1 mm), so that the junction, when moved, touches the wall first.

The location of the thermocouple probe is designed to coincide with that of the heat transfer measurement. However, when it moves downstream, increased flow speed can band the probe tube and cause difference between the location of heat transfer measurement and the probe.

3.1.3. Five-axis measurement unit

To determine the heat flux from the temperature gradient near the wall, temperatures should be measured in a direction normal to the wall with high precision. As mentioned previously, it is critical to know the location of the wall to determine its temperature accurately. The uncertainty in the measurement of the positions of the probe and the wall should be small to compare heat and mass transfer results at the same location on the endwall. To achieve this purpose, a five-axis measurement unit has been designed to locate the probe at specified positions and to measure temperatures above and perpendicular to the wall. The wall position is monitored by a programmable limit switch in a motion controller. It consists of four unislides ('x', 'y', 'z', and 'n'), one rotating table ('θ' in Fig. 3), a supporter and a modified five-axis motion controller. The thickness of the sublayer in the thermal boundary layer is generally about 500 μm at $Re_{ex} = 2 \times 10^5$, while the measurement system has a resolution of 5 μm. Thus, the resolution is two orders of magnitude smaller than the thickness of the thermal boundary layer. The five-axis system is connected to a supporter to reduce vibrations from the wind tunnel. The probe is attached to the z-axis slide and connected to an electrical circuit to find the wall position. When the probe touches the wall, it closes the electrical circuit and recognizes the wall position. Since the resolution of the unislide is 5 μm, the wall position is located with position error in the range of ±2.5 μm. For the heat transfer measurement, 140 positions are carefully chosen to measure heat transfer data from the heat transfer endwall, as shown in Fig. 4.

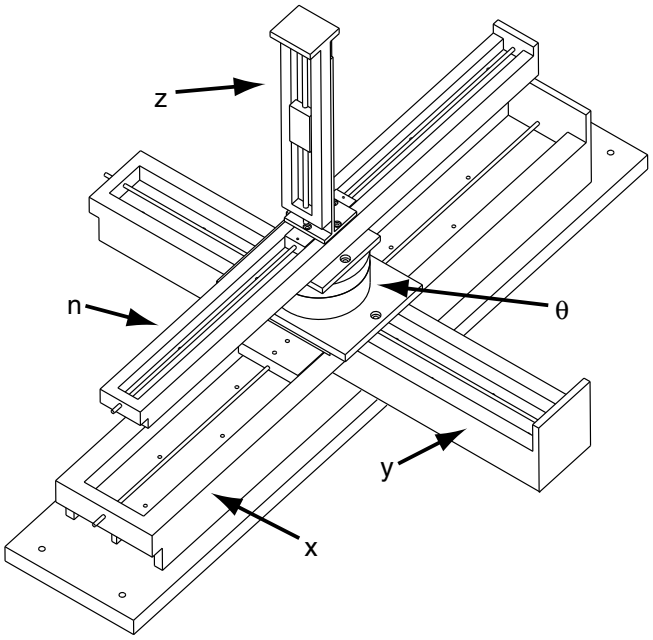

Fig. 3. Five-axis measurement unit sketch.

3.1.4. Heat transfer endwall and temperature control unit

The complicated secondary flows (cf. Fig. 5) in a turbine cascade induce large thermal gradients over the turbine endwall. Therefore, a major challenge in this heat transfer experiment is to maintain a constant wall temperature boundary condition. The following key steps were followed to design the heat transfer endwall. The active (heated) portion of the endwall was designed based on a simulation using a commercial CFD software. It has 128 Kapton strip heaters and 138 E-type thermocouples. Three different heaters are used: 12.8 × 12.8 mm;38.4 × 12.8 mm;192× 12.8 mm. Each heater has one E-type thermocouple except that the 192 × 12.8 mm size heater has three thermocouples. The locations of the heaters and thermocouples are shown in Fig. 6. The locations of the thermocouples are marked by 'plus' symbols. The heat transfer endwall only covers one passage between the third and the fourth blades. Fig. 7 shows the cross section of the heat transfer endwall. It consists of a aluminum plate having a thickness of 5 mm, Kapton strip heaters, E-type thermocouples, a balsa wood plate, and a phenolic insulated plate.

Heat transfer experiments with the constant temperature condition require a large number of heaters and temperature feedback in the system. Each heater needs at least one thermocouple to measure temperature and a power supply to maintain a constant temperature. The heat transfer endwall in the current system has 128 heaters and therefore requires 128 individually temperature control units. Therefore, a computer-controlled power supply with 128 output channels was developed at the Heat Transfer Laboratory, University of Minnesota.

3.2. Mass transfer experiment

The naphthalene sublimation technique is used to obtain local mass transfer results on the mass transfer endwall. The detailed description of this technique is provided by Goldstein and Cho [5].

3.2.1. Naphthalene sublimation method

The method consists of preparing the naphthalene test section, scanning the initial surface, conducting a wind tunnel experiment, and scanning the final surface. The test surface is prepared by casting to guarantee repeatability. A constant wall concentration condition in mass transfer is equivalent to a constant wall temperature condition in heat transfer, and a non-coated surface corresponds to an adiabatic wall condition. If the surface is maintained at a uniform temperature, the naphthalene vapor pressure and concentration will be uniform. Subsequently, the boundary

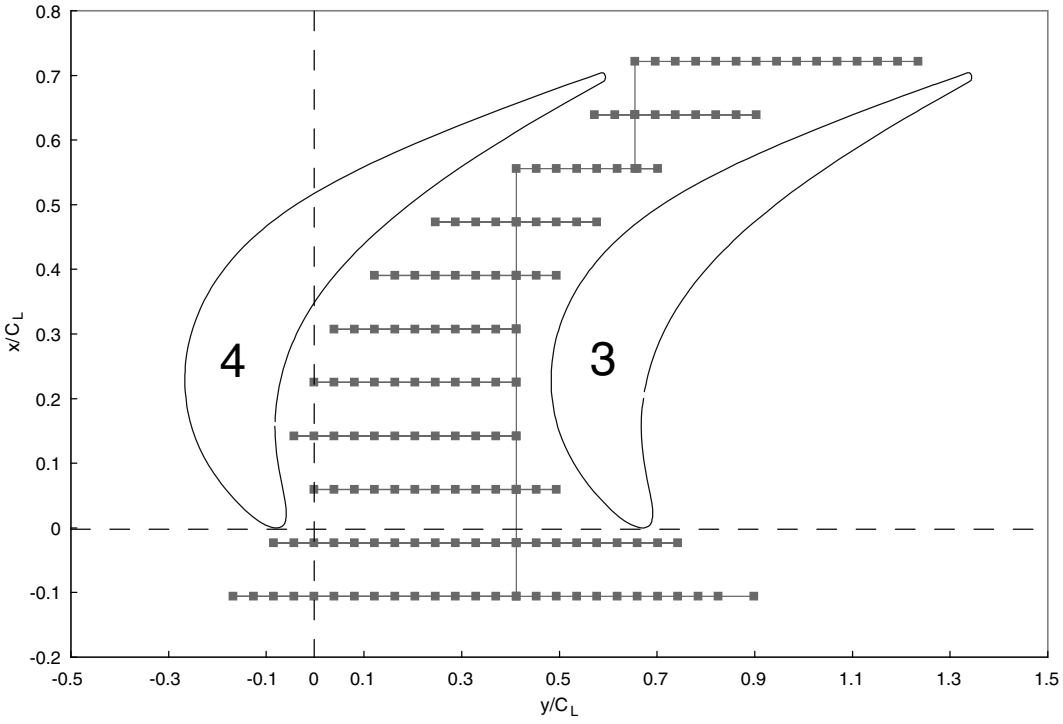

Fig. 4. Endwall measurement positions for heat transfer experiments.

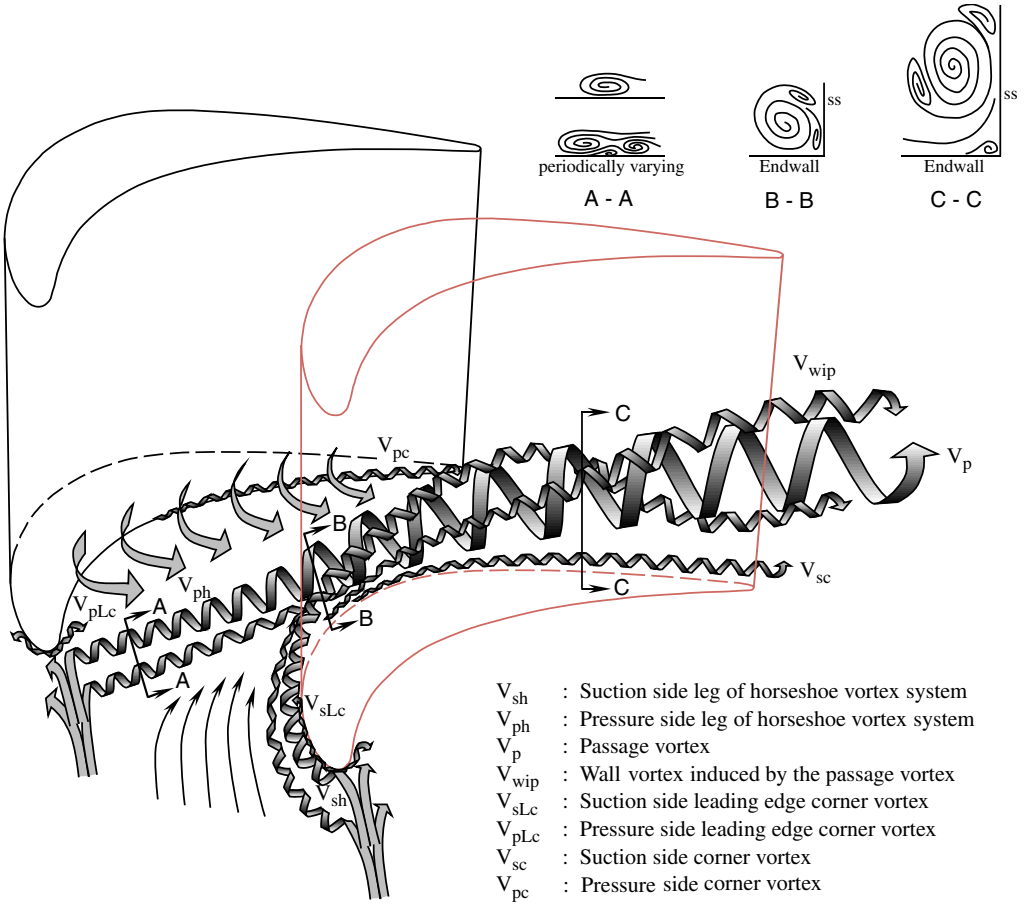

Fig. 5. Vortex model in turbine cascades from Wang et al. [18].

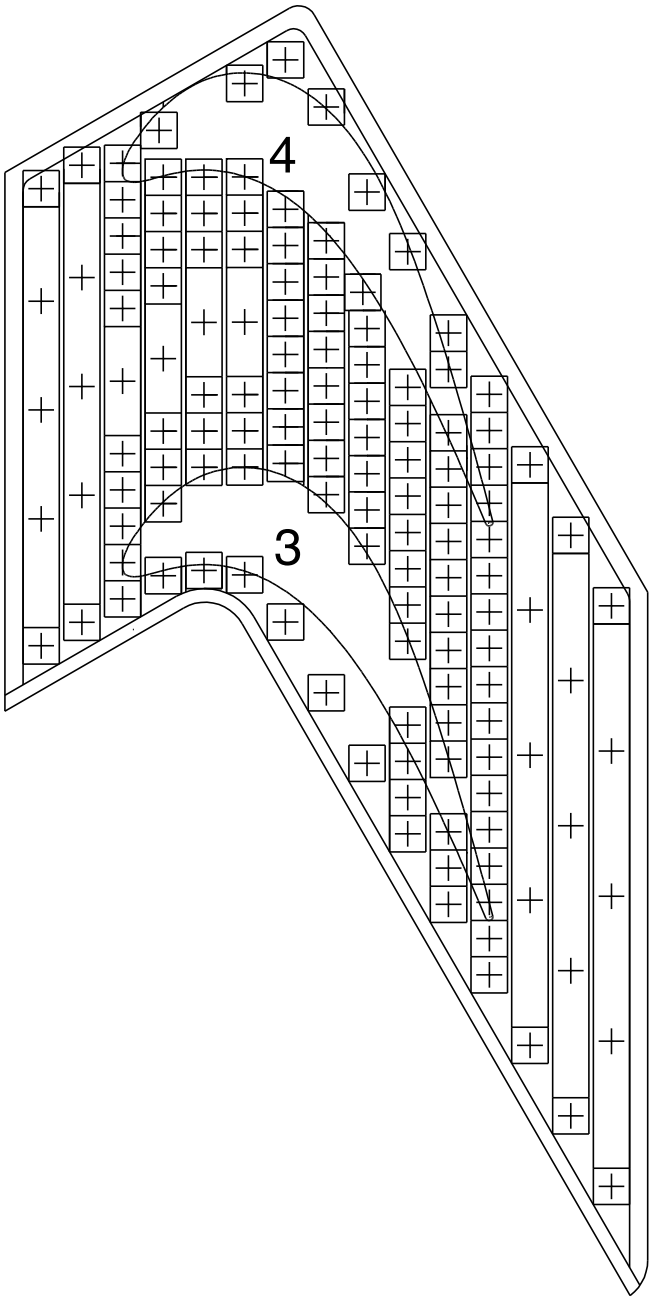

Fig. 6. Constant temperature endwall with heaters and thermocouples locations.

condition is equivalent to a constant wall temperature condition in heat transfer.

The mass diffusion coefficient of naphthalene in air ($0.0681\ \mathrm{cm^2/s}$) is obtained as the average of the values from Cho [12] ($0.066\ \mathrm{cm^2/s}$) and Chen and Wung [13] ($0.0702\ \mathrm{cm^2/s}$) at 298.16 K. In addition, Cho[12] states that the humidity does not significantly affect the diffusion coefficient of naphthalene in air. The saturation vapor density, $\rho_{\mathrm{v,w}}$, is calculated from the perfect gas law Eq. (14).

$$\rho_{\mathrm{v,w}} = \frac{p_{\mathrm{v,w}}}{RT_{\mathrm{n,w}}} = \frac{M_{\mathrm{naph}} p_{\mathrm{v,w}}}{\overline{R} T_{\mathrm{n,w}}}, \tag{14}$$

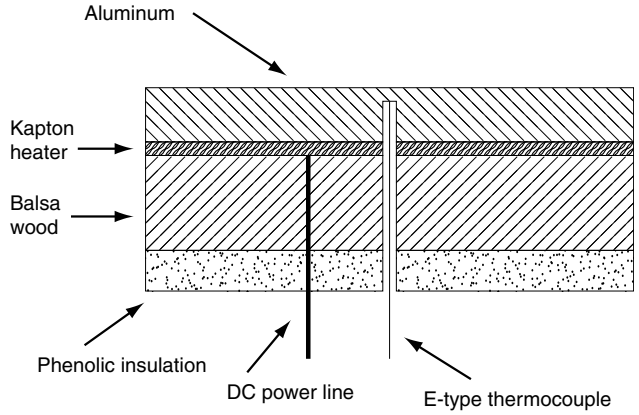

Fig. 7. Typical cross section of the constant temperature endwall.

where $T_{\mathrm{n,w}}$ is the surface temperature and $p_{\mathrm{v,w}}$ is the saturation vapor pressure. The latter is obtained from a correlation by Ambrose et al. [14]. As the saturated vapor pressure is very sensitive to temperature, it is necessary to control the temperature of the naphthalene surface very carefully. Subsequently, the mass transfer coefficient is determined from

$$h_{\mathrm{m}} = \frac{\dot{m}}{\rho_{\mathrm{v,w}} - \rho_{w,\infty}} = \frac{\rho_s \delta t / \delta \tau}{\rho_{\mathrm{v,w}}}, \tag{15}$$

where $\rho_{\mathrm{v,w}}$ is the vapor concentration at an impermeable wall and $\rho_{v,\infty} = 0$ for the mainstream.

From the mass transfer coefficient and diffusion coefficient, the Sherwood number can be expressed as

$$Sh = \frac{h_{\mathrm{m}} C_l}{D_{\mathrm{naph}}}. \tag{16}$$

The uncertainty level of the Sherwood number in the naphthalene sublimation technique using the methodology described in Coleman and Steele [15] is estimated to be approximately 7% at the 95% confidence level ($\pm 2\sigma$). The uncertainty of mass transfer coefficient not including that of the diffusion coefficient is 5.2%, which includes those of naphthalene vapor density and saturated vapor pressure.

3.2.2. Mass transfer endwall and measurement equipment

The mass transfer endwall, machined from aluminum, has a reservoir 2.54 mm deep to hold naphthalene. The side rims have a 5 mm width to provide reference points. The rims of the mass transfer endwall are highly polished to enhance the repeatability of the measurements. To align two separate measurement points before and after the wind tunnel experiment, a small reference point is drilled into the reference rim surface. Three holes for three E-type thermocouples are drilled into the reservoir so that the surface temperature of naphthalene can be monitored during each experiment. To ensure a smooth surface in the casting method, a highly polished cover plate is prepared. Two holes are drilled inside of the reservoir: a vent hole and the injection hole for the molten naphthalene. Since the

mass transfer endwall is larger, additional bolts and nuts are used to prevent the lifting of the cover plate in the center of the endwall. Otherwise, the naphthalene liquid leaks into the gap between the endwall and the cover plate, leading the LVDT to go out of range during the surface scanning. After the naphthalene liquid is poured into the setup, it is solidified in the mold and makes the test endwall. Unlike the heat transfer endwall, the mass transfer endwall (Fig. 8) covers two passages in the turbine cascade.

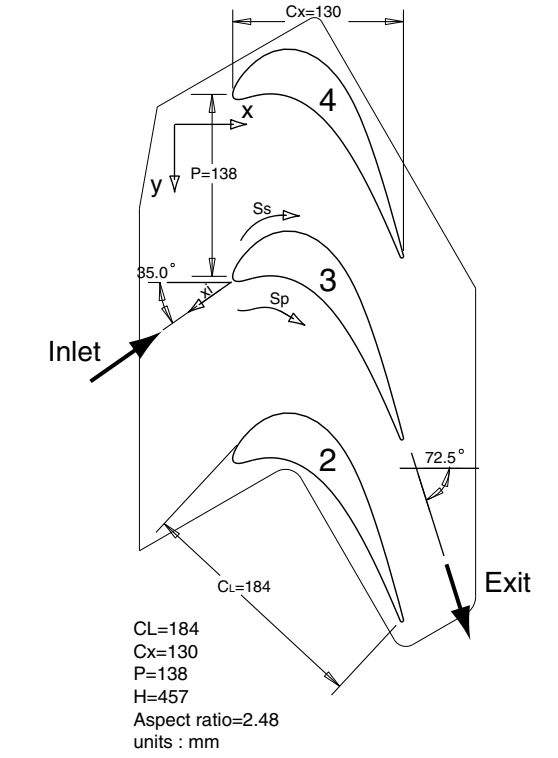

(a) heat transfer

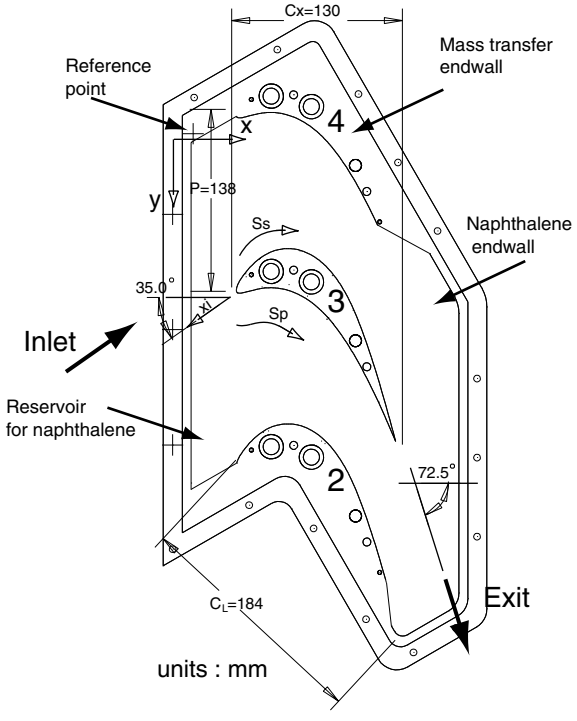

(b) mass transfer

Fig. 8. Blades configuration on the heat and mass transfer endwalls.

An automated scanning system is used to measure the sublimation depth in the mass transfer experiments. It consists of two unislides and one motion controller. The current system, cf. Fig. 9, can take measurement at five thousand locations in one hour. The sublimation depth is about 60 μm, and therefore a careful alignment of the reference point is crucial to get reliable data. Before each surface scanning, the reference point is found and set to zero by the linear voltage displacement transformer (LVDT) and the motion controller.

4. Results and discussion

To evaluate the analogy factor on a turbine endwall, heat transfer and mass transfer experiments are conducted with equivalent experimental and geometrical conditions. In this paper, local mass transfer and heat transfer results on the endwall are compared using the heat/mass transfer analogy.

4.1. Mass transfer results

For the mass transfer experiments, the endwall is active (subliming), whereas the blades are not. The mass transfer results are presented to investigate the performance of a leading edge modification, as described in Han and Goldstein [16]. Four different mass transfer experiments were conducted: two Reynolds numbers (4.38×10^5 and 5.77×10^5) with a low turbulence intensity (0.2%), and two Reynolds numbers (4.27×10^5 and 5.67×10^5) with a high turbulence intensity (8.5%). The high turbulence intensity in the flow is generated using a bar grid and measured with a hot-wire anemometer. The experimental conditions for mass transfer are listed in Table 2.

For detailed local measurements, 5000 locations are selected to cover two flow passages on the mass transfer surface. The run time of the mass transfer experiment in the wind tunnel depends on the flow velocity and is chosen to provide ≈ 60 μm as the average sublimation loss.

To quantify the results from the mass transfer experiment, they are compared with the results from Goldstein and Spores [17] upstream of the leading edge. Fig. 10 shows that the horseshoe vortex and the leading edge corner vortex are closely located compared with the earlier results (obtained with a different blade geometry) and shows only one peak point for all cases, while the Stanton number from the earlier tests show two peaks. The current blade has a small and sharp leading edge, but the earlier tests were done on a blade with a blunt leading edge. It is reasonable to think that the current design generates relatively

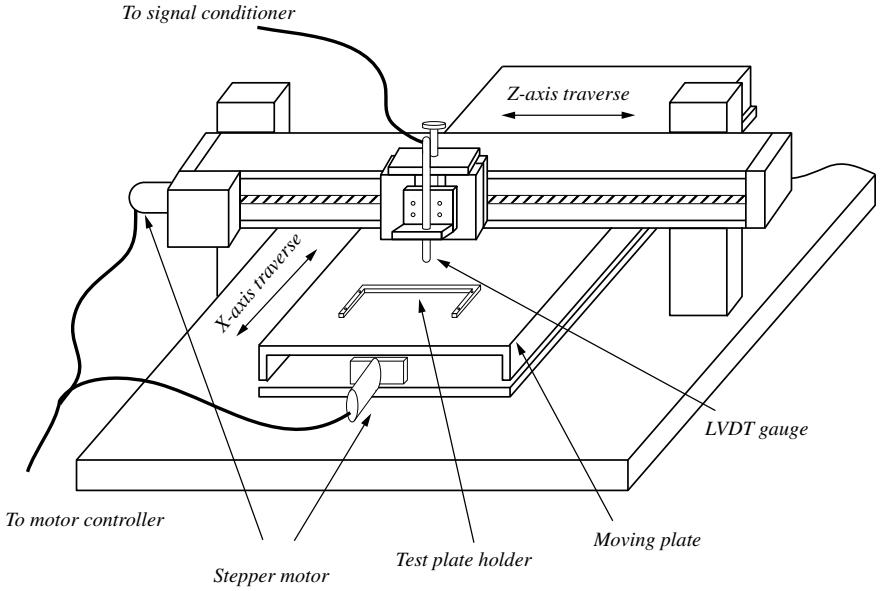

Fig. 9. Schematic of mass transfer endwall measurement table.

Table 2
Mass transfer experimental conditions on the endwall

No	Run	Trip wire (mm)	Re_{ex}	U_{ex} (m/s)	Tu (%)
1	MT-Run15	1.0	4.38×10^5	38.5	0.2
2	MT-Run11	1.0	5.77×10^5	50.6	0.2
3	MT-Run17	1.0	4.27×10^5	37.4	8.5
4	MT-Run19	1.0	5.67×10^5	49.9	8.5

a small horseshoe vortex close to the leading edge corner vortex.

The influence of the passage vortex, horseshoe vortex, leading edge corner vortices, and second corner vortices are observed in Fig. 11. As mentioned in Han and Goldstein [16], high turbulence reduces the development of the passage vortex and horseshoe vortex, cf. Fig. 12. The Sherwood numbers from the mass transfer experiments are normalized for the verification of the heat/mass transfer analogy by $Re^{1/2}$. Regardless of the Reynolds number, normalized Sherwood number distributions show similar results. Therefore, only MT-Run15 and MT-Run17 are shown in Figs. 11 and 12.

4.2. Heat transfer results

For the heat transfer measurements, three different cases are investigated. To establish an equivalent condition to

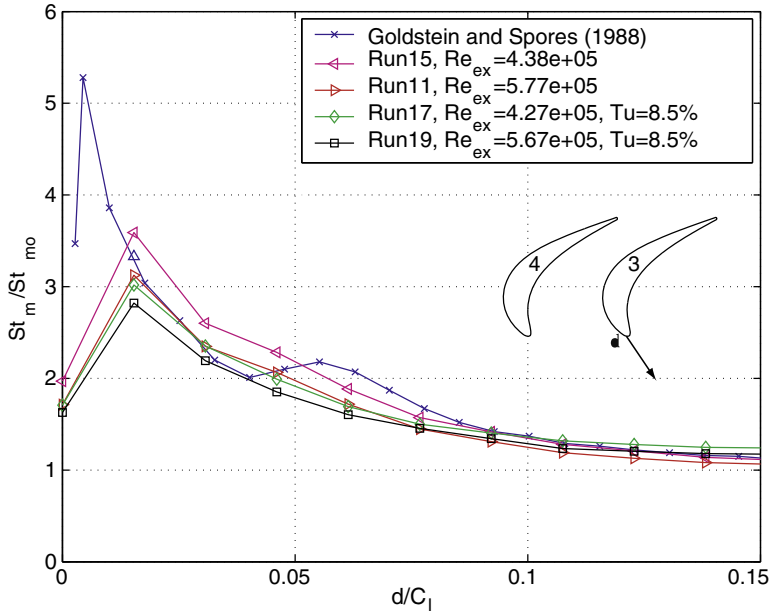

Fig. 10. *St* number comparison in front of a leading edge.

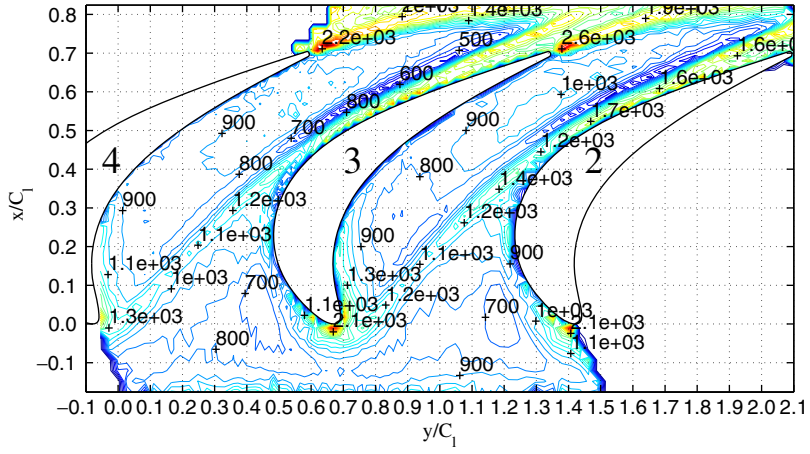

Fig. 11. Sherwood number contour plot with $Re_{ex} = 4.38 \times 10^5$ and $Tu = 0.2\%$ from Han and Goldstein [16].

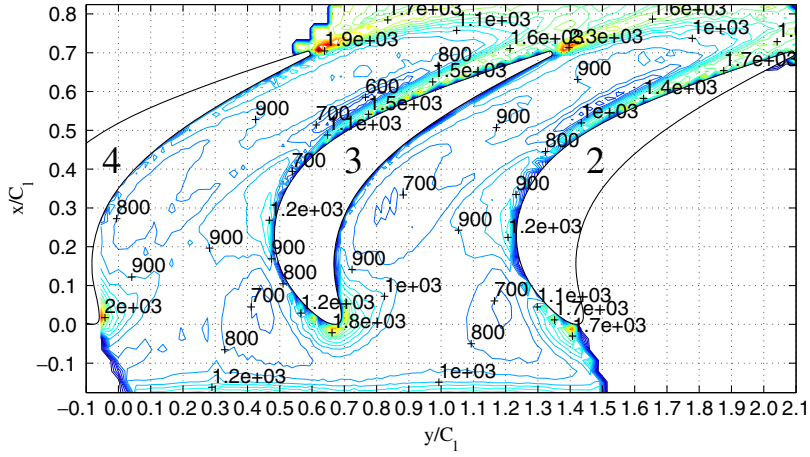

Fig. 12. Sherwood number contour plot with $Re_{ex} = 4.27 \times 10^5$ and $Tu = 8.5\%$ from Han and Goldstein [16].

Table 3
Heat transfer experimental conditions on the endwall

No	Run	Trip wire (mm)	Re_{ex}	U_{ex} (m/s)	Tu (%)
1	HT-Run11	1.0	2.56×10^5	21.6	0.2
2	HT-Run12	1.0	1.95×10^5	16.2	0.2
3	HT-Run13	1.0	2.29×10^5	19.6	8.5

the mass transfer experiment, the endwall is maintained at a constant temperature, while the blades are approximately adiabatic. The heat transfer experiments employ smaller Reynolds number than the mass transfer experiments to prevent excessive probe vibration and misalignment due to bending. The heat transfer results are partially presented to show the thermal boundary layer measurement technique in Han and Goldstein [10]. The experimental conditions are listed in Table 3.

After each thermal boundary layer is measured at the heat transfer endwall, the thermal gradient is carefully evaluated in the linear conduction region. In addition, the wall and mainstream flow temperatures are required to evaluate the Nusselt number. The wall temperature is determined by extrapolating the linear (least square) fit line in the conduction region to its intersection with the wall position. The wall position is determined by the motion controller to a precision of 2.5 μm. The uncertainties in the temperature gradient and the Nusselt numbers are evaluated from the measured temperatures. The uncertainty of the gradient depends on the boundary layer thickness and fluctuation of the flow. Each measurement position has a thermal boundary layer profile similar to the one shown in Fig. 13.

The local Nusselt numbers from the heat transfer experiments are plotted as contour graphs, as labeled in Figs. 14 and 15. They show the Nusselt number distributions from HT-Run11 and HT-Run13, respectively. Since HT-Run12 does not show significant difference from HT-Run11, it is not presented here. Unlike the mass transfer figures, it is difficult to see here the development of vortices due to the smaller number of measurement points (140 vs. 5000) in the contour plots. There is a shortage of measurements near the blades, due to the probe design and efforts to avoid breaking the probe. Therefore, high heat transfer regions by the passage vortex, pressure and suction corner vortices are not clearly observed. However, the high heat

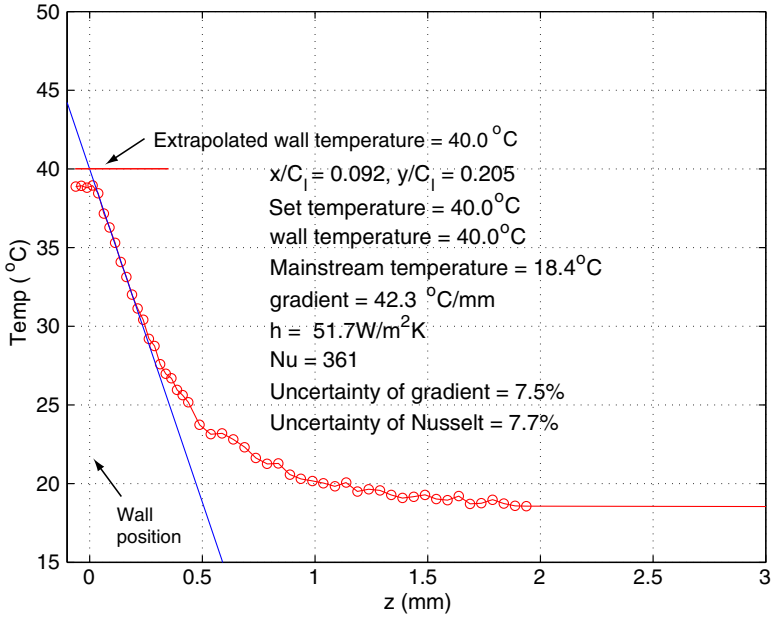

Fig. 13. Sample thermal boundary layer profile on the endwall.

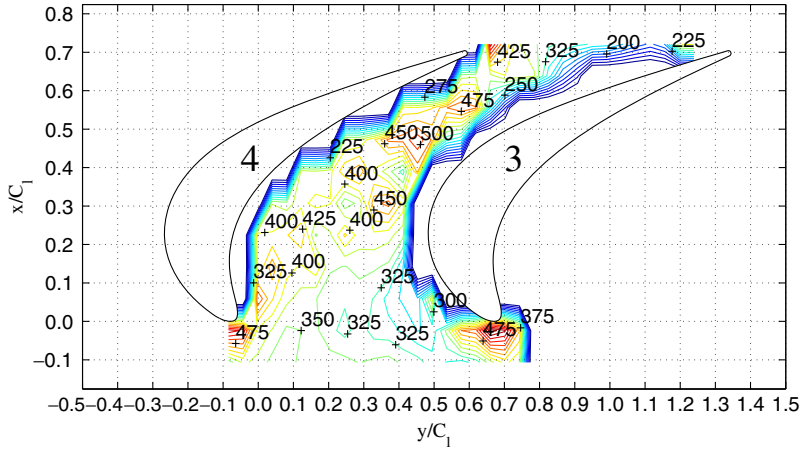

Fig. 14. Nusselt number contour plot with $Re_{ex} = 2.56 \times 10^5$ and $Tu = 0.2\%$ from Han and Goldstein [10].

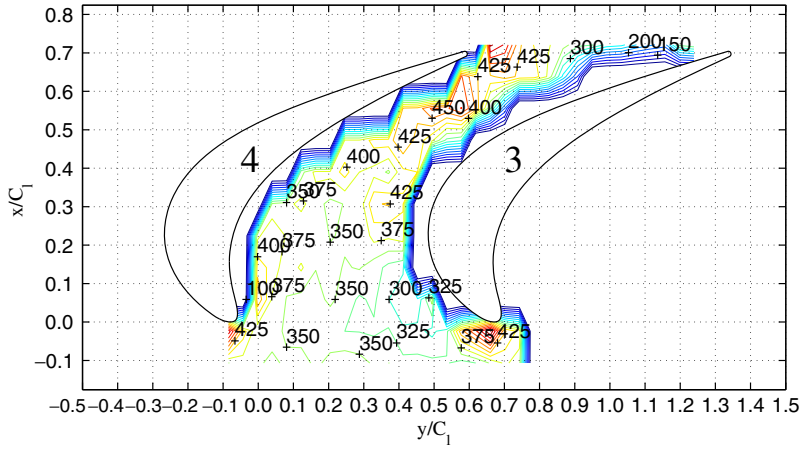

Fig. 15. Nusselt number contour plot with $Re_{ex} = 2.29 \times 10^5$ and $Tu = 8.5\%$ from Han and Goldstein [10].

transfer region by the horseshoe vortices near the leading edge is well observed in these plots. The Nusselt numbers from the heat transfer experiments are normalized for the heat/mass transfer analogy by $Re^{1/2}$.

4.3. Heat/mass transfer analogy factor

Expressions for the heat/mass transfer analogy factor (Eqs. (8) and (10)) are not convenient for data comparison. Consequently, the Nusselt and Sherwood numbers are expressed using the Prandtl and Schmidt numbers and an exponent 'n', as in Eq. (6). Thus for the comparison, we assume that the Nusselt number is expressed as

$$Nu = f(x)Re_x^m Pr^n \tag{17}$$

and the Sherwood number is determined from

$$Sh = f(x)Re_x^m Sc^n, \tag{18}$$

where $f(x)$ is a function for a certain geometry. The analogy factor is evaluated using Eqs. (17) and (18). The com-

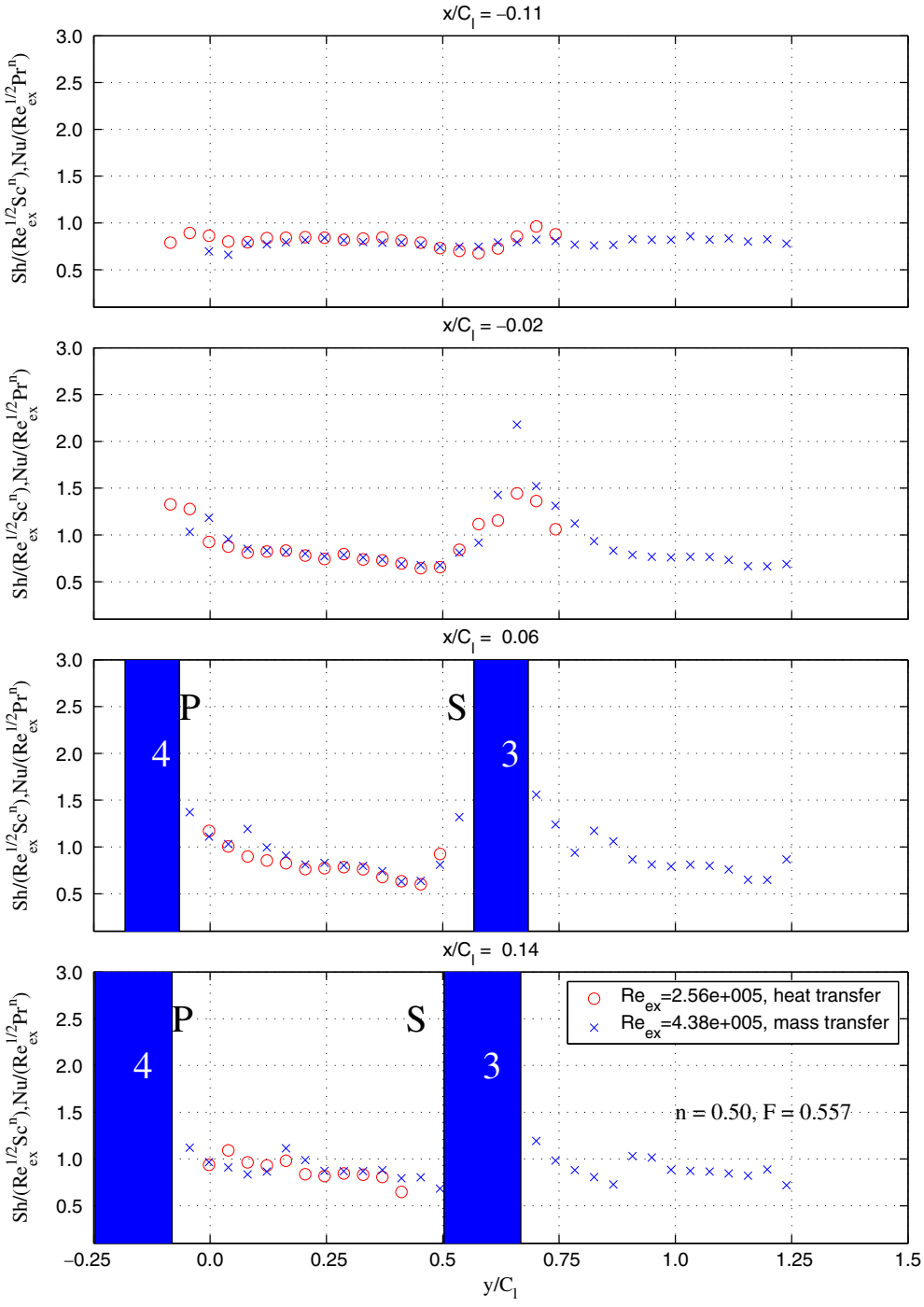

Fig. 16. Heat and mass transfer analogy plot 1 with $n = 0.5$ and $Tu = 0.2\%$.

parison between heat and mass transfer results require not only equivalent experimental conditions, but also the same measurement positions. With the smaller number of measurement locations in the heat transfer studies, Sherwood numbers from the mass transfer experiments are interpolated to get values at the measurement locations (cf. Fig. 4) corresponding heat transfer experiment.

The two-dimensional plots from Figs. 16–21 show the heat/mass transfer coefficients for these experiments. The rectangular bars represent the turbine blades and change in width with streamwise positions. The numbers inside the rectangular bars represent the blade number. The letter 'P' means the pressure side and the letter 'S' means the suction side. Normalized Nusselt numbers are shown between the third and the fourth blade and normalized Sherwood numbers are shown between the third and the fifth blade.

Because of the different Reynolds number in the experiments, the Nusselt and Sherwood numbers are normalized

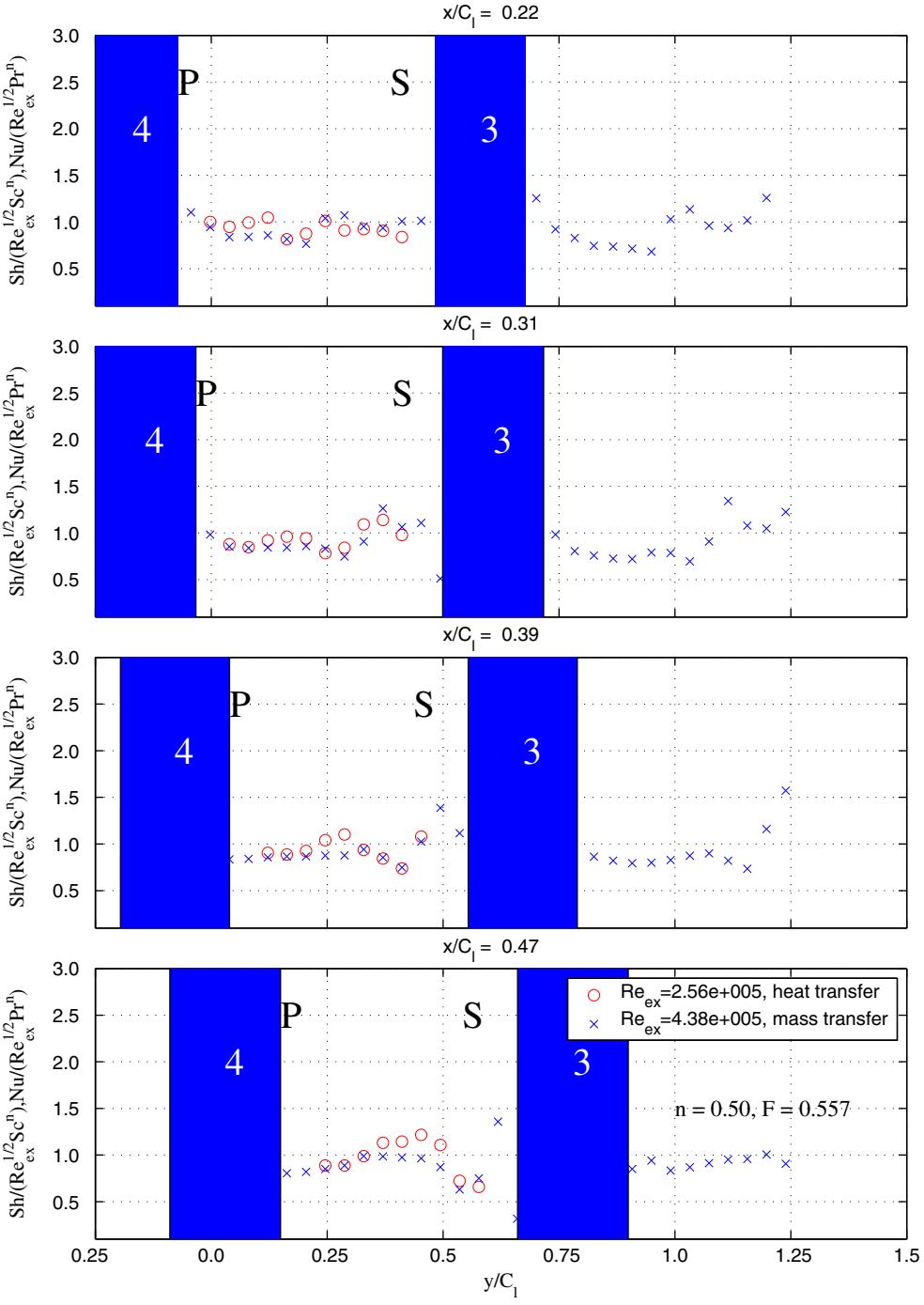

Fig. 17. Heat and mass transfer analogy plot 2 with $n = 0.5$ and $Tu = 0.2\%$.

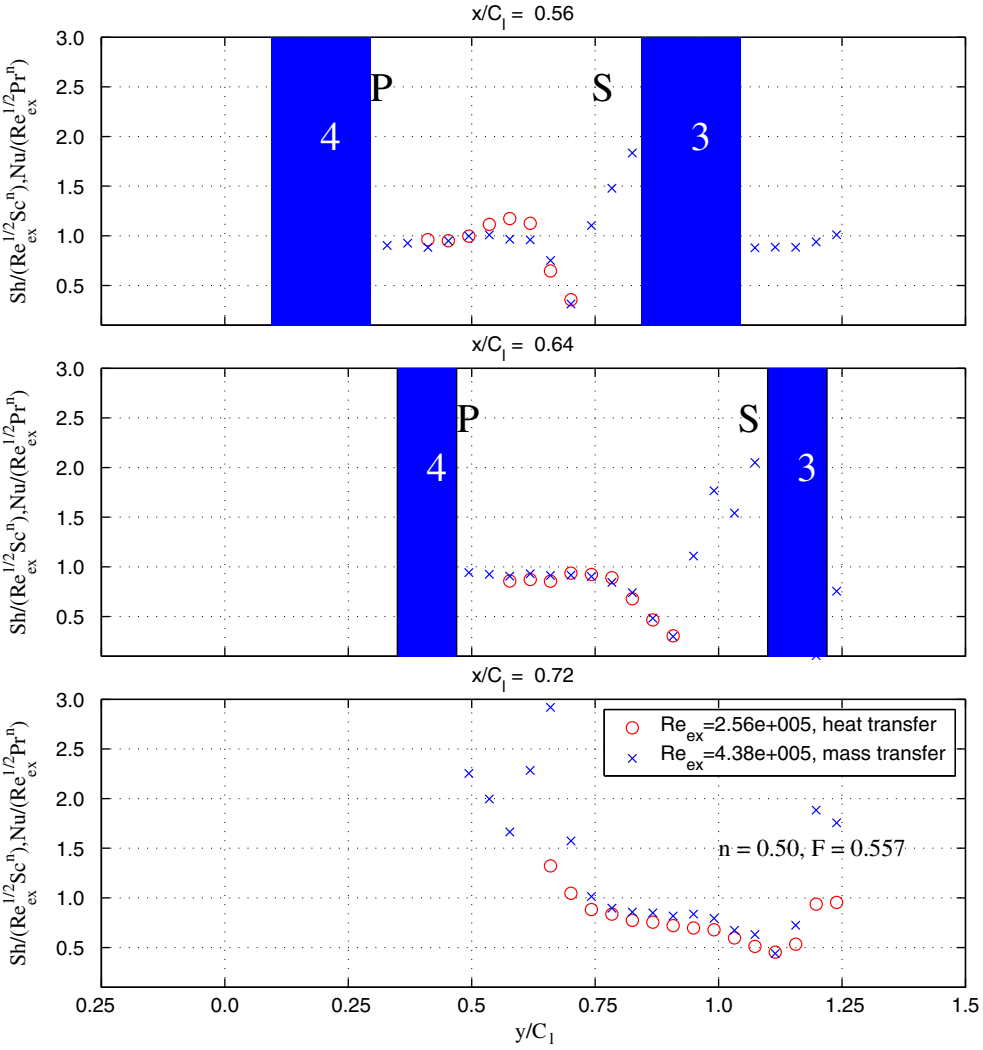

Fig. 18. Heat and mass transfer analogy plot 3 with $n = 0.5$ and $Tu = 0.2\%$.

using Re^m with $m = 1/2$. The normalized Nusselt and Sherwood numbers are adjusted using $(Pr/Sc)^n$, where $Pr = 0.707$ and $Sc = 2.28$. By varying 'n' from 1/3 to 1.0, $n = 0.5(F = 0.557)$ provides a good agreement between the results of two type experiments.

From Figs. 16–18 the heat transfer results (HT-Run11) and mass transfer results (MT-Run15) with low turbulence intensity ($Tu = 0.2\%$) are shown together at different streamwise positions in a normalized form. Immediately upstream of the leading edge $(x/C_l = -0.02, y/C_l = 0.60)$ and immediately downstream of the trailing edge $(x/C_l = 0.72, y/C_l = 0.12)$, the mass transfer results are higher than the heat transfer results with $n = 0.5$ $(F = 0.557)$. At all other locations, the comparison with $n = 0.5$ $(F = 0.557)$ shows a good agreement between the heat and mass transfer results. At $x/C_l = 0.56$ and 0.64, heat transfer results near the suction surface are not available due to the size of the probe. Therefore, the analogy is not verified over the regions which are covered by much of the passage vortex.

From Figs. 19–21 results from a heat transfer experiment (HT-Run13) and a mass transfer experiment (MT-Run17) with high turbulence intensity ($Tu = 8.5\%$) are shown together. The high turbulence intensity result shows a good agreement with $n = 0.5(F = 0.557)$, much like the low turbulence study. The comparison shows a difference near the stagnation point $(x/C_l = -0.02, y/C_l = 0.60)$ and after the trailing edge $(x/C_l = 0.72)$. As in the low turbulence case, the heat transfer results near the suction surface are not available at $x/C_l = 0.56$ and 0.64. At $x/C_l = 0.72$, the heat transfer results do not agree well with the mass transfer results. This may be due to the vibration and misalignment of the probe in the high turbulence flow. Another possibility is the limitation of mass transfer measurement. The comparison of heat transfer measurements between low turbulence and high turbulence intensity shows no difference after the trailing edge $(x/C_l = 0.72)$. However, the comparison of mass transfer measurements between low turbulence and high turbulence intensity does. Therefore, there is a chance that mass transfer data with

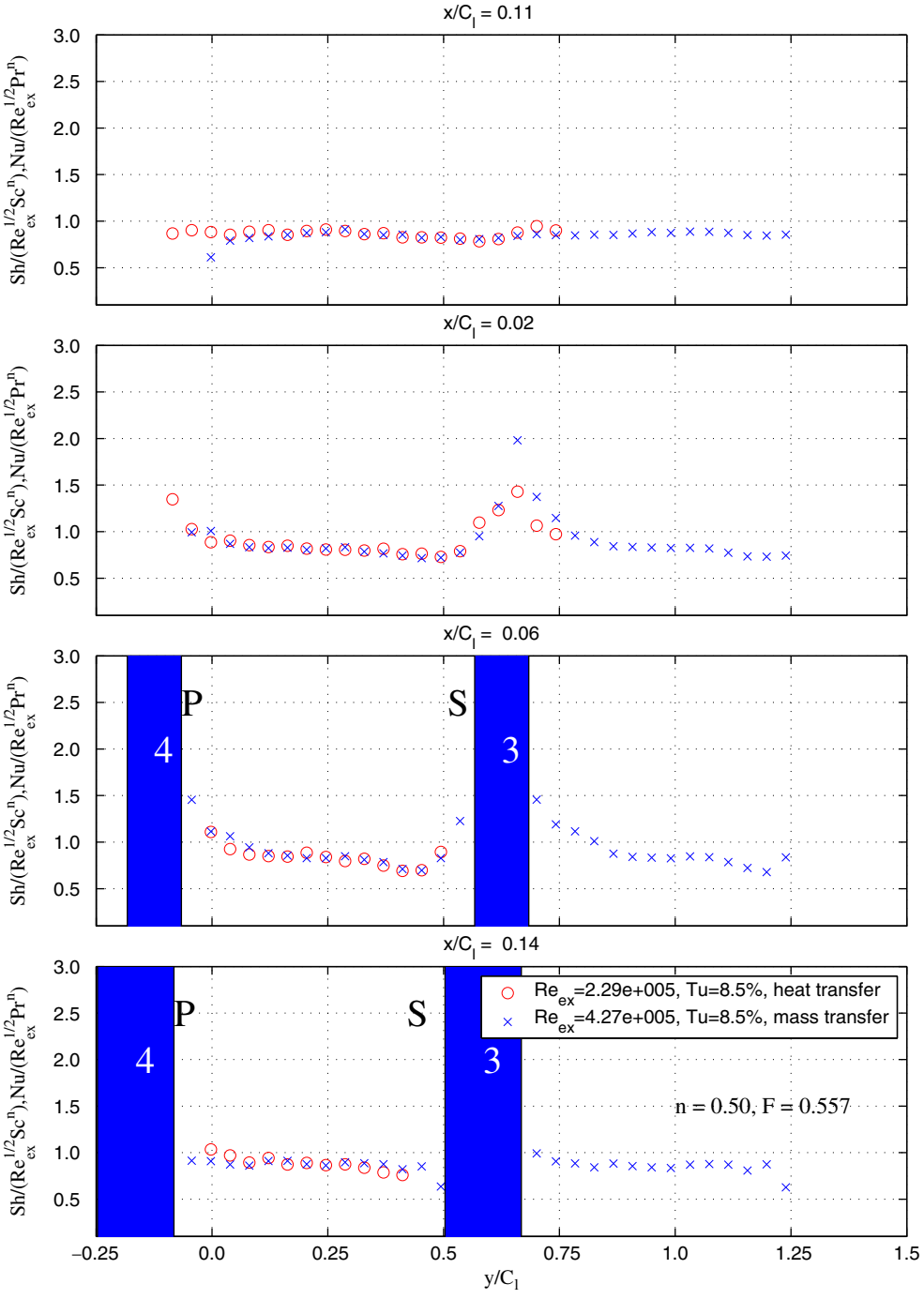

Fig. 19. Heat and mass transfer analogy plot 1 with $n = 0.5$ and $Tu = 8.5\%$.

high turbulence intensity is not properly evaluated after the trailing edge ($x/C_l = 0.72$). Generally the high turbulence intensity results are not significantly different from the low turbulence intensity results. In the developed turbulent boundary layer on the endwall, an analogy factor of $n = 0.5 (F = 0.557)$ (Figs. 16–21) shows a good agreement with the turbulent cases in Goldstein and Cho [5].

Due to the conduction error of the probe in large thermal gradient regions, the heat transfer measurement does not measure the temperature accurately in the very high heat transfer regions, near the stagnation point ($x/C_l = -0.02, y/C_l = 0.60$) and after the trailing edge ($x/C_l = 0.72, y/C_l = 1.20$). Except for these locations, the conduction error is negligible. This difference in the heat and mass transfer experiments may result from the difference between the normalized Nusselt number and Sherwood number in high heat transfer regions, which are along the leading and the trailing edges where the flow is very complex. Another possibility is the misalignment of the thermal probe. Even though the position is controlled

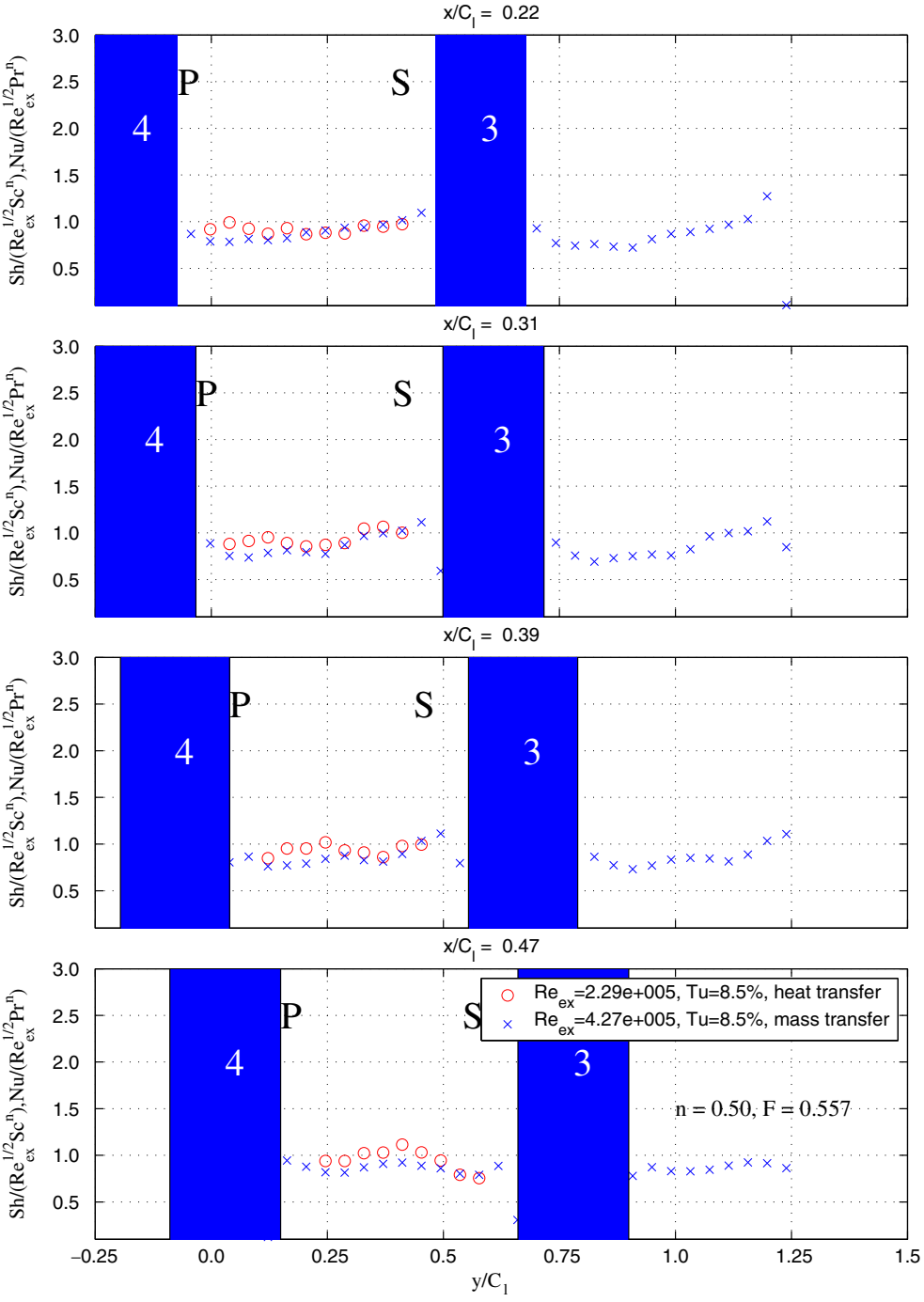

Fig. 20. Heat and mass transfer analogy plot 2 with $n = 0.5$ and $Tu = 8.5\%$.

by the motion controller and computer, the probe is bent by the incoming flow in the wind tunnel, as explained earlier. (The exit flow has a 2.72 times larger velocity than the incoming flow.) As the probe moves downstream, larger flow velocities can increase the misalignment.

5. Conclusions

A series of heat and mass transfer experiments have been conducted to investigate the heat and mass transfer analogy on the endwall in a simulated turbine cascade with direct concern for the influence of Reynolds number and high turbulence intensity. To show the validity of the heat and mass transfer analogy on an endwall, heat and mass transfer experiments have been conducted with boundary conditions.

For simplicity in the comparison, the heat and mass transfer data are expressed by $Nu/(Re_x^{1/2}Pr^n)$ with $Pr = 0.707$ and $Sh/(Re_x^{1/2}Sc^n)$ with $Sc = 2.28$, respectively. For the endwall experiment, '$n = 0.5$' ($F = 0.557$) generally

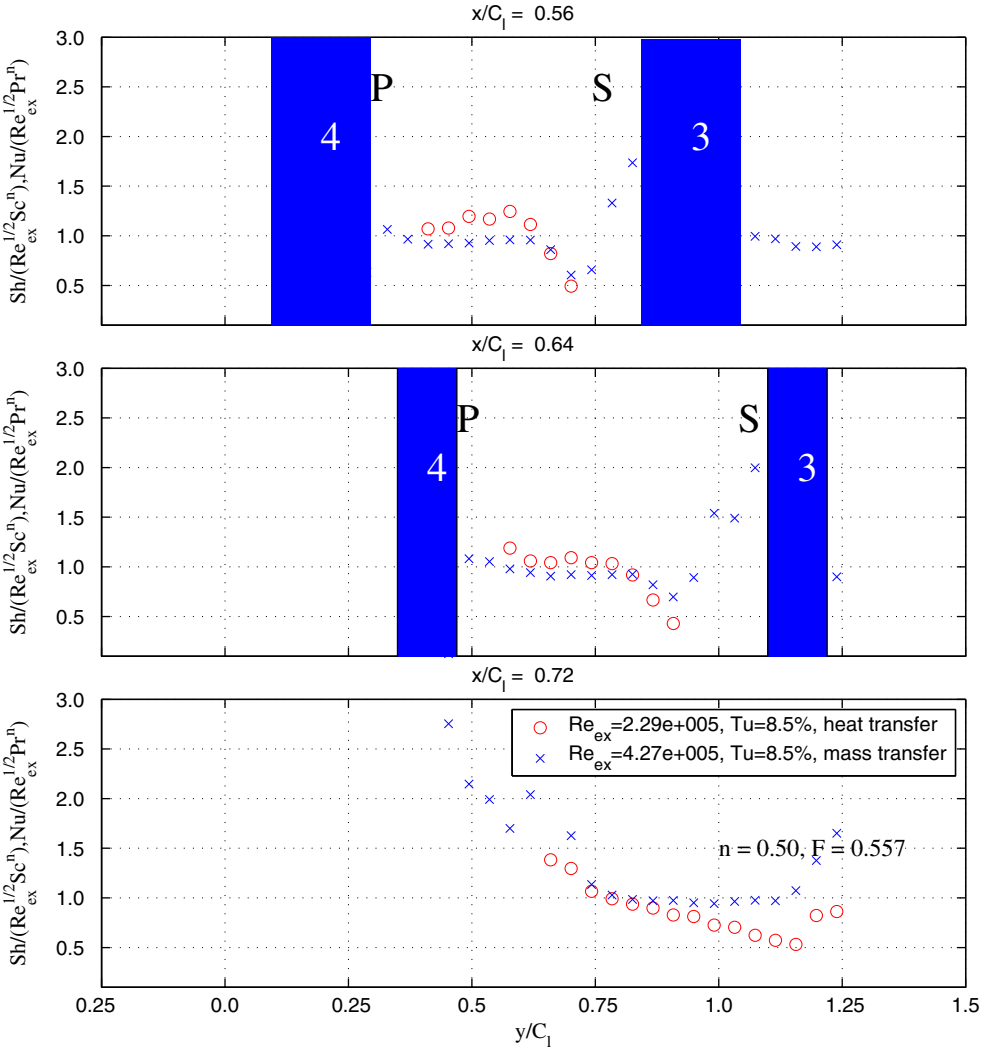

Fig. 21. Heat and mass transfer analogy plot 3 with $n = 0.5$ and $Tu = 8.5\%$.

matches heat and mass transfer data with the heat/mass transfer analogy regardless of turbulence intensity and Reynolds number within the range studied. Unlike the case on the blade in the companion paper, the flow does not experience the development from laminar to turbulence and '*n*' does not change over the test section. The disagreement in the comparisons between the heat and mass transfer results occurs in high heat transfer regions perhaps due to limitations of the heat transfer measurement technique. The analogy is not verified in the regions where the passage vortex approaches the blade, because of lack of data. In addition, the effect of the increased turbulence intensity does not change the heat/mass transfer comparison with the tripped boundary layer.

Acknowledgements

The authors would like to acknowledge DOE for their support. This research was performed with financial support (02-01-SR096) from University Turbine System Research Program.

References

[1] W. Nusselt, Wärmeübergang, diffusion und verdunstung, Math. Mechanik 2 (1930) 105–121.
[2] E. Schmidt, Verdunstung und wärmeügergang, Gesundheits-Ingenieur 29 (1929) 525–529.
[3] J.S. Lewis, A heat/mass transfer analogy applied to fully developed turbulent flow in an annulus, J. Mech. Eng. Sci. 13 (4) (1971) 286–292.
[4] P.H. Chen, R.J. Goldstein, Convective transport phenomena on the suction surface of a turbine blade including the influence of secondary flows near the endwall, J. Turbomach. 114 (1992) 776–787.
[5] R.J. Goldstein, H.H. Cho, A review of mass transfer measurements using naphthalene sublimation, Exp. Therm. Fluid Sci. 10 (1995) 416–434.
[6] E.R.G. Eckert, H. Sakamoto, T.W. Simon, The heat/mass transfer analogy factor, nu/sh, for boundary layers on turbine blade profiles, Int. J. Heat Mass Transfer 44 (2001) 1223–1233.
[7] S.-Y. Yoo, J.-H. Park, C.-H. Chung, M.-K. Chung, An experimental study on heat/mass transfer from a rectangular cylinder, J. Heat Transfer 125 (2003) 1163–1169.
[8] E.R.G. Eckert, R.M. Drake, Analysis of Heat and Mass Transfer, McGraw-Hill, New York, 1972.
[9] W.M. Kays, M.E. Crawford, Convective Heat and Mass Transfer, third ed., McGraw-Hill, New York, 1993.

[10] S. Han, R. Goldstein, Heat transfer study in a linear turbine cascade using a thermal boundary layer measurement technique, ASME J. Heat Transfer 129 (10) (2007) 1384–1394.
[11] B.F. Blackwell, R.J. Moffat, Design and construction of a low velocity boundary temperature probe, J. Heat Transfer 97 (2) (1975) 313–315.
[12] K. Cho, Measurement of the diffusion coefficient of naphthalene into air, Ph.D. Thesis, State Univ. New York at Stony Brook, 1989.
[13] P.H. Chen, P.H. Wung, Diffusion coefficient of naphthalene in air at room temperature, personal communication.
[14] D. Ambrose, I. Lawrenson, C. Sparke, The vapor pressure of naphthalene, J. Chem, Thermodyn. 7 (1975) 1173–1176.
[15] H.W. Coleman, W.G. Steele, Experimentation and Uncertainty Analysis for Engineers, second ed., A Wiley-Inerscience Publication, 1999.
[16] S. Han, R. Goldstein, Influence of blade leading edge geometry on turbine endwall heat (mass) transfer, ASME J. Turbomach. 128 (2006) 798–813.
[17] R.J. Goldstein, R.A. Spores, Turbulent transport on the endwall in the region between adjacent turbine blades, J. Heat Transfer (1988) 862–869.
[18] H.P. Wang, S.J. Olson, R.J. Goldstein, E.R.G. Eckert, Flow visualization in a linear turbine cascade of high performance turbine blades, ASME J. Turbomach. 119 (1997) 1–8.